A Five-Axis Monolithic Nanopositioning Stage Constructed from a Bimorph Piezoelectric Sheet

Meysam Omidbeike, Yuen K. Yong, Steven I. Moore, Andrew J. Fleming

***Abstract*— The paper describes design, modeling and control of a five-axis monolithic nanopositioning stage constructed from a bimorph piezoelectric sheet. In this design, actuators are created by removing parts of the sheet using ultrasonic machining. The constructed nanopositioner is ultra-compact with a thickness of 1 mm. It has a X and Y travel range of 15.5 μm and 13.2 μm respectively; a Z travel range of 26 μm; and a rotational motion about the X- and Y-axis of 600 μrad and 884 μrad respectively. The first resonance frequency occurs at 883 Hz in the Z-axis, and the second and third resonance frequency appears at 1850 Hz, rotating about the X- and Y-axis. A decentralized control strategy is implemented to track Z, θ_x and θ_y motions. The controller provides good tracking and significantly reduces cross-coupling motions among the three degrees-of-freedom.**

I. Introduction

Nanopositioning systems are devices used extensively in applications requiring sub-nanometer resolutions [1]–[3]. Applications include atomic force microscopy [4]–[6], data storage [7], nanofabrication [8], [9], cell surgery [10] and precision optics [11].

The piezoelectric tube scanner has been one of the most commonly used nanopositioner in scanning probe microscopy [12], [13]. This class of monolithic nanopositioners is economical, easy to fabricate and can provide up to three degrees of freedom (DOF) motion with sub-nanometer resolution. However, to achieve large travel range, a long piezoelectric tube is required. This results in a lower resonance frequency and significant cross-coupling between the lateral and vertical directions [13], [14].

In the last decade, piezoelectric tube scanners have been replaced by flexure-based nanopositioners in atomic force microscopy in order to improve scan speed and reduce cross-coupling motions among all axes [15], [16]. The moving platforms of these high-speed positioning devices are guided by metal flexures and driven by piezoelectric stack actuators [3], [16], [17]. The high stiffness of flexures in the out-of-plane directions significantly reduces cross-coupling motion and allows for a higher payload than monolithic devices. There are many commercial available flexure-based nanopositioner designs ranging from one-DOF to six-DOF [18]. However, these designs are more costly, heavier, and bulkier than monolithic devices especially for positioners with high DOFs [1].

Authors are with the Precision Mechatronics Lab, Faculty of Engineering and Built Environment, The University of Newcastle, Callaghan 2308, New South Wales, Australia. {meysam.omidbeike, yuenkuan.Yong, Steven.i.moore, andrew.fleming}@newcastle.edu.au.net

A new class of monolithic nanopositioner constructed from a single piezoelectric sheet was proposed in [1], [19], [20]. In these two-DOF monolithic nanopositioners, parts of the sheet are removed to create active flexures which are used to simultaneously drive and guide the moving platform along the X- and Y-axis. These devices have the lowest profile for nanopositioning stages yet with a thickness of within 500 μm to 1.5 mm. The extremely thin design of the nanopositioner enables a new range of applications in atomic force microscopy, and particularly, scanning electron microscopy where the load-lock area may be less than 5 mm in height [21]. This work proposes a new design which extends the DOFs of the previously proposed monolithic nanopositioners from two to five. The five DOFs include three translational motions along the X-, Y- and Z-axis, and two rotational motions about the X- and Y-axis. The five-axis monolithic nanopositioner is constructed from a bimorph sheet of piezoelectric material which has a thickness of only 1 mm. Ultrasonic machining is used to remove piezoelectric material to create a series of bimorph flexures and electrode features. The bimorph flexures are connected to a moving platform, and there are served as actuators as well as mechanical guides to the platform. By driving the bimorph flexures with a combination of voltages, the flexures provide in-plane and out-of-plane bendings which in turns generating the five-axis of motions.

The remainder of the paper precedes as follows. Section II describes the design of the monolithic stage and the actuating principles for generating the five DOFs. Section III presents the analytical models which describe the relationship between force/deflection and the applied voltage, effective stiffness, effective mass and resonance frequency for each DOF. Finite-element simulations are presented in Section IV, followed by experimental results in Section V. SectionVI presents a decentralized control strategy to improve tracking and reduce cross-coupling effect in closed-loop. Section VII concludes the paper.

II. Design

The bimorph monolithic nanopositioner is illustrated in Fig. 5. The nanopositioner is fabricated from a bimorph piezoelectric sheet of PZT-5A with sputter-coated 5 μm Nickel electrodes. The dimension of the piezoelectric sheet is 72.3 mm$\times$72.3 mm$\times$1 mm. The mechanical and electrode features were created by ultrasonic machining of the bimorph sheet. The final shape and critical dimensions of the nanopositioner are illustrated in Fig. 1. The electrode features were

978-1-7281-0948-0/19/$31.00 ©2019 IEEE

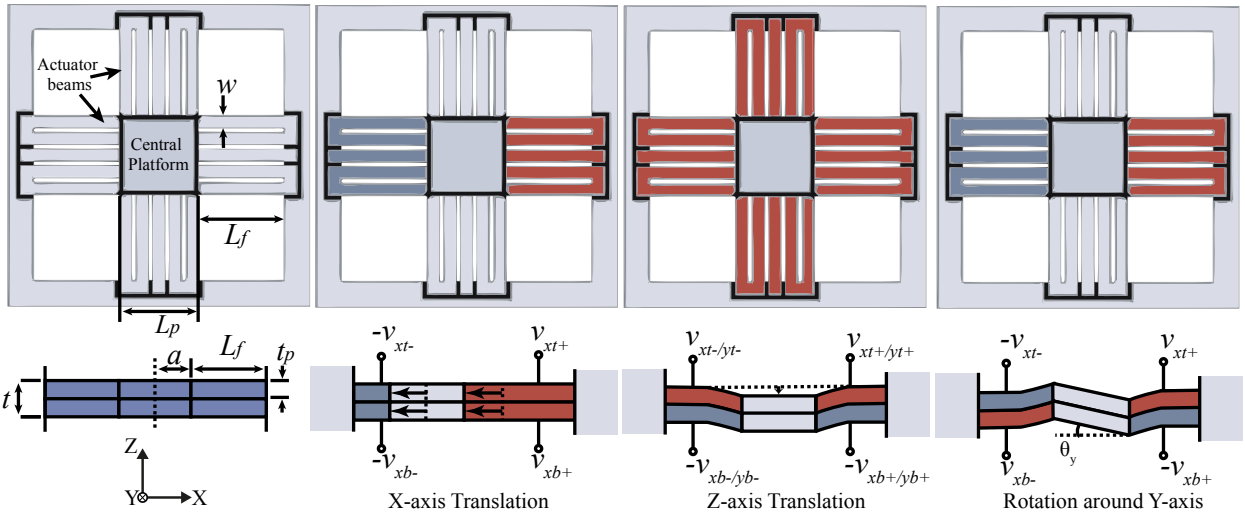

Fig. 1. From the left: Parameters of the bimorph stage; X-axis translation and the corresponding applied voltages; Z-axis translation and the corresponding applied voltages; Rotational motion about the Y-axis and the corresponding applied voltages.

created on both top and bottom surfaces while the middle layer is grounded.

The actuating principles for generating the five DOF motions are shown in Fig. 1. Assuming that each layer is outwardly poled and with middle layer grounded, a positive voltage applied to the top and bottom surface will cause the beam to expand and displace the central platform away from the positive voltage. For example, when a positive voltage is applied to the v_{xt+} and v_{xb+} electrode, and an equal and opposite voltage is applied to the v_{xt-} and v_{xb-} the central platform will translate in the negative X-direction.

III. Modeling

In this section, a static model is derived to describe the relationship between force/deflection and the applied voltage for each DOF. The effective stiffness and effective mass for each DOF are also derived for estimating the corresponding resonance frequency. Fig. 1 shows the parameters used in the analytical equations.

A. Translational DOF along the X/Y-axis

The generated force, effective stiffness and deflection of the stage for this DOF have been derived in [1]. There are,

$$F_x = Nd_{31}k_xV, \quad k_x = N\frac{c^EA}{L_f}, \quad \delta_x = \frac{L_fd_{31}}{t_p}V. \tag{1}$$

where N is the number of actuator beams, d_{31} is the piezoelectric strain constant, c^E is the Young's modulus of elasticity, A is the cross-sectional area, L_f is the actuator's length, t_p is the thickness of each piezoelectric layer, and V is the applied voltage. With the given dimensions and material properties in Table I, the estimated static gain along the X and Y axes is 15.6 nm/V.

Effective mass of an extended beam can be estimated as $0.23\rho AL_f$ [22]. Thus, the total effective mass is

$$M_{e,\delta x} = N\left(0.23\rho AL_f\right) + m_p, \tag{2}$$

TABLE I

Dimensions and material properties of the bimorph stage.

Description	Parameter	Value
Thickness of a single piezoelectric layer, mm	t_p	0.5
Thickness of the bimorph sheet, mm	t	1.0
Actuator beam length, mm	L_f	20
Length of platform, mm	L_p	19
Half-length of platform, mm	a	9
Width of actuator beam, mm	w	3
Young's modulus, GPa	c^E	66
Poisson's ratio	v	0.35
Density, kg/m^3	ρ	7800
Piezoelectric constant, pm/V	d_{31}	-190

where $m_p = 2\rho L_p^2t_p$ is the mass of the platform, and ρ is the material density. With the known effective mass and stiffness calculated in (1) and (2), the resonance frequency along the X and Y axes is estimated to be 18.2 kHz.

B. Translational DOF along the Z-axis

A fixed-guided beam as shown in Fig. 2 is used to derive the analytical equations for this DOF. For a bimorph piezoelectric bender, the constitutive equations for the two layers are [23],

$$\text{Upper layer,} \quad S_1 = s_{11}^ET_1 - d_{31}E_3, \tag{3}$$
$$\text{Lower layer,} \quad S_1 = s_{11}^ET_1 + d_{31}E_3, \tag{4}$$

where S_1 and T_1 are the strain and stress along the length of the bender, E_3 is the electric field, and $s_{11}^E = 1/c^E$ is the elastic compliance. Substituting $S_1 = z\kappa$ into (3) and (4), where κ is the curvature, and z is the distance to the neutral axis of the bender, gives

$$\text{Upper layer,} \quad T_1 = c_{11}^E\kappa z + c^Ed_{31}E_3, \tag{5}$$
$$\text{Lower layer,} \quad T_1 = c_{11}^E\kappa z - c^Ed_{31}E_3, \tag{6}$$

For an elementary area dA, the elementary moment dM caused by the force normal to dA is $dM = zdF$, and

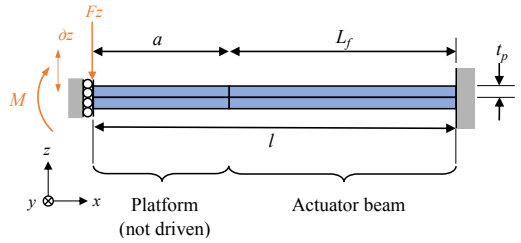

Fig. 2. An actuated bimorph beam along the X-axis where its right-hand end is fixed and its left-hand end is guided.

$dF = T_1 dA = T_1 w dz$, where w is the width of the beam. Thus,

$$dM = T_1 w z dz. \tag{7}$$

Substituting (5) and (6) into (7), the bending moment can be expressed as,

$$M = \int_{-t_p}^{0} \left(c^E \kappa z - c^E d_{31} E_3\right) w z dz + \int_{0}^{t_p} \left(c^E \kappa z + c^E d_{31} E_3\right) w z dz. \tag{8}$$

Solving the above equation gives,

$$M = \frac{t_p^2 w c^E \left(3E_3 d_{31} + 2\kappa t_p\right)}{3}. \tag{9}$$

Rearranging and substituting $E_3 = V/t_p$ into (9), we obtain the curvature of the actuator beam as

$$\kappa = \frac{3}{2c^E t_p^3 w} M - \frac{3d_{31}}{2t_p^2} V = \alpha M - \beta V, \tag{10}$$

where $\alpha = \frac{3}{2c^E t_p^3 w}$ and $\beta = \frac{3d_{31}}{2t_p^2}$. From (10), it can be seen that the bending curvature of the bimorph actuator is related to the moment and applied voltage.

Fig. 2 shows a bimorph beam with a fixed-guided boundary condition. The deflection of the bimorph beam under the applied voltage V and moment M is estimated by double integrating the bending curvature, which gives

$$\begin{aligned} \delta z(x) &= \iint \kappa dx = \int_0^{L_f} (\alpha M x - \beta V x) dx \\ &= \frac{L_f^2}{2}(\alpha M - \beta V), \end{aligned} \tag{11}$$

According to Roark's formulas [24], the deflection and the moment at the guided-end of the beam is

$$\delta z = \frac{-F_z L_f^3}{12 c^E I_y}, \quad M = \frac{F_z L_f}{2}. \tag{12}$$

where $I_y = wt^3/12$. Substituting (12) into (19), F_z can be expressed as,

$$F_z = \frac{18 c^E I_y d_{31} t_p w}{L_f \left(2wt_p^3 + 9I_y\right)} V, \tag{13}$$

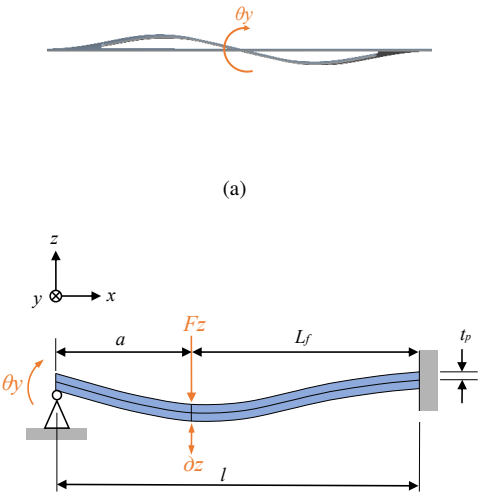

Fig. 3. (a) Side-view of the stage showing its rotational motion about the Y-axis. (b) The bimorph beam is one-half of the planar stage along the X-axis where it is fixed on the right-hand end and pinned on the left-hand end.

and the stiffness of the bimorph beam along the Z-axis can be expressed as

$$k_z = \left|\frac{F_z}{\delta z}\right| = \frac{12 c^E I_y}{L_f^3}. \tag{14}$$

There are 20 actuator beams in total. Using (13) and (14), the total effective force and stiffness are

$$F_{e,\delta z} = 20 F_z, \quad K_{e,\delta z} = 20 k_z. \tag{15}$$

The deflection of the platform is therefore

$$\delta z = \frac{F_{e,\delta z}}{K_{e,\delta z}} = \frac{F_z}{k_z}. \tag{16}$$

which is calculated to be 59.9 nm/V.

The effective mass of the stage can be obtained using the Rayleigh's principle as reported in [1]. The total effective mass is

$$M_{e,\delta z} = 20\left(\frac{13}{35} m_b\right) + m_p. \tag{17}$$

where $m_b = \rho w t_p L_f$ is the mass of the actuator beam, and m_p is the mass of the platform. Using (15) and (17), the resonance frequency along the Z-axis is calculated to be 1082 Hz.

C. Rotational DOF about the X/Y-axis

A fixed-pinned boundary condition is considered for the rotational DOF about the X/Y-axis of a single beam, as shown in Fig. 3. Due to symmetry, the derivation for both axes is the same, thus only θ_y is shown here. θ_y can be found by finding δ_z at $x = a$ as shown in the figure, and estimating θ_y using geometry,

$$\theta_y = \arctan\left(\frac{\delta z}{a}\right) \times \frac{180^\circ}{\pi}. \tag{18}$$

The deflection of the fixed-pinned beam at any value of x can be derived by double integrating (10) as follows,

$$\begin{aligned}\delta z(x) &= \int_0^l \alpha M x dx - \int_0^{L_f} \beta V x dx \\ &= \frac{\alpha l^2}{2} M - \frac{\beta L_f^2}{2} V, \end{aligned} \tag{19}$$

where $l = a + L_f$. Note that the integration of $\beta V x$ is performed over the length L_f where the voltage is applied. The deflection and moment at $x = a$ for the fixed-pinned boundary condition are [24],

$$\delta z(a) = \frac{F_z a^3 (a-l)^2 (a+2l)}{12 c^E I_y l^3} - \frac{F_z a^2 (a-l)^2}{4 c^E I_y l}, \tag{20}$$

$$M(a) = \frac{F_z a (l-a)^2 (2l+a)}{2l^3}. \tag{21}$$

Substituting (20) and (21) into (19), F_z can be expressed as

$$F_z = \frac{18 c^E I_y V d_{31} l^3 t_p w \left(a+l\right)}{a \left(a-l\right) \sigma}, \tag{22}$$

where

$\sigma = -2wa^3 t_p^3 - 4wa^2 l t_p^3 + 6wal^2 t_p^3 + 9 I_y a l^2 + 18 I_y l^3$. From (20), the effective stiffness of the actuator beam at $x = a$ is

$$k_z = \frac{12 c^E I_y l^3}{a^2 (a-l)^3 (a+3l)}, \tag{23}$$

Using (23) and ignoring the beams that are perpendicularly aligned to those under studied, the total effective stiffness of the stage is

$$K_{e,\delta z} = 10 k_z, \tag{24}$$

and the deflection of the platform at $x = a$ is

$$\delta_z(a) = \frac{F_{e,\delta z}}{K_{e,\delta z}} = \frac{10 F_z}{10 k_z} = \frac{F_z}{k_z}. \tag{25}$$

Substituting (25) into (18), θ_y is estimated to be 2.4 μrad/V.

The effective mass of the stage is estimated using the Rayleigh's principle [25],

$$m_e = \rho A \int_L \left[\frac{z\left(x\right)}{z_{max}}\right]^2 dx, \tag{26}$$

where A is the cross-sectional area of the beam, $z\left(x\right)$ is the shape function (vibration amplitude) of the beam, and z_{max} is the maximum displacement of the beam along the Z-direction. The shape function for the fixed-pinned beam for $x > a$, as shown in Fig. 3, is

$$z\left(x > a\right) = \frac{F_z a}{12 c^E I_y l^3} \left(l - x\right)^2 \left(3l^2 x - a^2 x - 2a^2 l\right), \tag{27}$$

The maximum displacement for the case of $a < 0.414l$ is [24]

$$z_{max} = \frac{F_z a \left(l^2 - a^2\right)^3}{3 c^E I_y \left(3l^2 - a^2\right)^2}. \tag{28}$$

Substituting (27) and (28) into (26), the effective mass for the actuator beam is $m_e = 0.4118 \rho A L_f$. The total effective mass is

$$M_e = 10 m_e + m_p. \tag{29}$$

TABLE II

PIEZOELECTRIC PROPERTIES FOR THE PZT-5A BIMORPH SHEET FROM PIEZO SYSTEM INC.

Piezoelectric coefficient, C/m^2		Relative permittivity, $\varepsilon = \varepsilon^S/\varepsilon_\circ$	
e_{31}	-10.92	ε_{11}	916
e_{33}	12.08	ε_{33}	830
e_{15}	12.29		

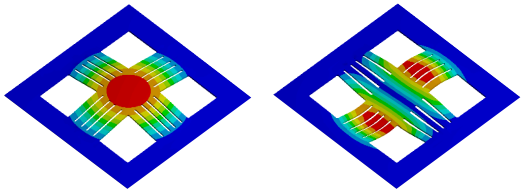

1st res. 883.5 Hz 2nd res. 1960.7 Hz

Fig. 4. Finite-element simulated resonance frequencies of the monolithic stage.

With the known effective stiffness (24) and mass (29), the stage is estimated to rotate about the X/Y-axis at a resonance frequency of 2407 Hz.

IV. FINITE-ELEMENT-ANALYSIS

A finite-element (FE) model of the bimorph planar stage was constructed using ANSYS workbench. Displacement of all four edges of the stage are fixed. The piezoelectricity of the stage is modeled using the ANSYS Piezo and MEMS Application Customization Toolkit (ACT) extension. The piezoelectric properties for PZT-5A is listed in Table II. Each piezoelectric layer is polarized outwards along its thickness direction. The middle of the bimorph is grounded.

To obtain the displacement per unit voltage for $\delta_{x/y/z}$ and $\theta_{x/y}$ along the X, Y and Z axes, +1 V and -1 V are applied to the corresponding electrodes for each DOF as shown in Fig. 1. The respective displacements are obtained. Table III compares the simulated and analytical static gains of the stage.

Resonance frequencies of the stage were simulated using the modal analysis module of ANSYS. The first two modes of the monolithic stage are shown in Fig. 4. The first resonance frequency appears at 883.5 Hz, translating along the Z-axis. The second and third mode is a rotational mode about the X-/Y-axis, occurs at 1960.7 Hz. To search for the lateral modes along the X and Y axes of the stage, the out-of-plane motions along the Z-axis were constrained. The X- and Y-axis lateral mode occurs at 21.26 kHz Simulated resonance frequencies are listed in Table III together with their analytical counterparts.

V. EXPERIMENTAL RESULTS

The experimental setup consists of a nanopositioner mounted on a base as pictured in Fig. 5. The translational motion in each axis is measured using MSA-3D interferometer. Rotational motions about the X- and Y-axis are measured using the Attocube interferometer. The Attocube rotational measurement is performed by mounting a mirror on each end

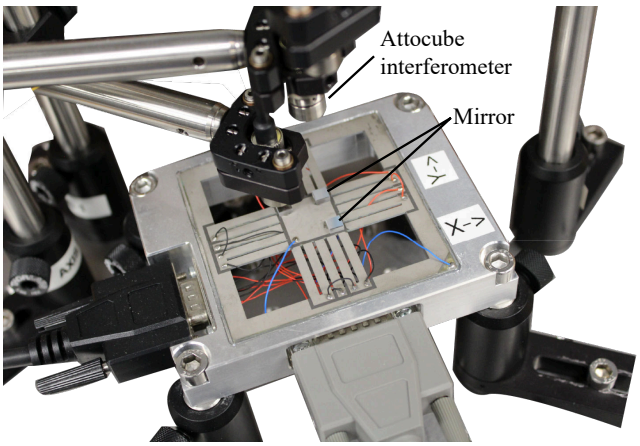

Fig. 5. Monolithic nanopositioner mounted on a base.

TABLE III
COMPARISON OF THE ANALYTICAL, FE-SIMULATED AND EXPERIMENTAL RESULTS

	Static gain		
	Analytical	FEA	Exp
X-Axis Translation (nm/V)	15.6	16.8	15.55
Y-Axis Translation (nm/V)	15.6	16.8	13.17
Z-Axis Translation (nm/V)	59.9	50	66.22
X-Axis Rotation (μrad/V)	2.4	2	1.5
Y-Axis Rotation (μrad/V)	2.4	2	2.2
	Resonance frequency (Hz)		
X/Y-Axis Translation	22071	21260	–
Z-Axis Translation	1082	883.5	845
X/Y-Axis Rotation	2407	1960.7	1850

of the platform. Measuring the vertical displacement on each side, the rotation of the platform can be calculated from (18). To evaluate the travel range, electrodes were driven with a 10-Hz sinusoidal voltage from -200 V to $+200$ V as shown in Fig. 1. Note that $+200$ V is only 20% of the positive range and was chosen conservatively to ensure a safe operating range for the material. The measured translational motions are 26.5 μm in the Z-axis, 6.22 μm in the X-axis and 5.27 μm in the Y-axis. The rotational motion is 600 μrad and 884 μrad about the X- and Y-axis respectively. Table III compares the analytical, FE-simulated and measured static gains of the monolithic stage. There are in close agreement to each other.

Fig. 6 shows the measured frequency responses of the stage. The frequency responses of the translational motions in the X- and Y-axis exhibits a relatively constant response over a wide frequency range. However, the maximum useful frequency is limited by the first resonance mode in the Z-axis occurring at 845 Hz. The measured rotational resonance mode for both θ_x and θ_y appears at 1850 Hz. The measured resonance frequencies are in close agreement with that of the FE simulations. The analytical resonances are approximately 22% larger than that of the experimental results. These discrepancies are due to the one-dimensional beam model. The discrepancy in the rotational mode are also due to the unmodeled beam actuators that are perpendicularly aligned to the axis of motion.

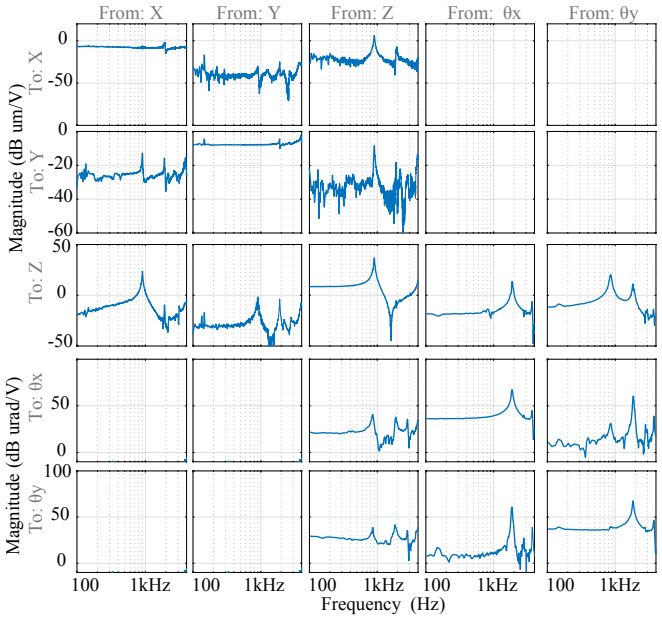

Fig. 6. The frequency response of the stage from the $\theta_{x/y}$, X-,Y- and Z-axis voltages to translational and rotational motions. The reference voltage is amplified by a gain of 50 before actuating the stage.

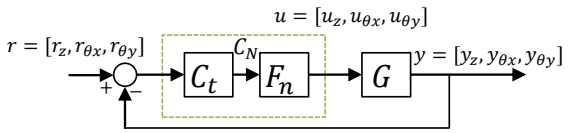

Fig. 7. Block diagram of the decentralized controller.

VI. DECENTRALIZED CONTROL

The performance of the nanopositioner in closed-loop is evaluated by implementing a decentralized control law. Here, the device is used as a vertical nanopositioner with three DOF motion in Z, θ_x and θ_y. For closed-loop control, a decentralized integral controller, and a decentralized integral and notch controller were implemented on a dSPACE-ds1103 board using Simulink coder. The vertical and rotational motions are measured using the three Attocube interferometers as shown in Fig. 5. The block diagram of the control law is shown in Fig. 7 where C_t is a diagonal integral controller, F_n is a diagonal notch filter and G is the plant. The diagonal controller can be written as

$$C_N(s) = diag\{C_N(s)\} = \begin{bmatrix} C_{Nz} & 0 & 0 \\ 0 & C_{N\theta x} & 0 \\ 0 & 0 & C_{N\theta y} \end{bmatrix}, \quad (30)$$

where the transfer function of diagonal elements is given by

$$C_N(s) = C_t F_n = \left(\frac{k_i}{s}\right) \frac{s^2 + 2\omega_n \zeta_n s + \omega_n^2}{(s+\omega_n)^2}. \quad (31)$$

The notch filters are tuned to the lowest resonance frequencies of the corresponding diagonal frequency responses in Fig. 6. For translation in the Z-axis, the notch filter is tuned to 845 Hz and for rotations about the X- and Y-axis, the

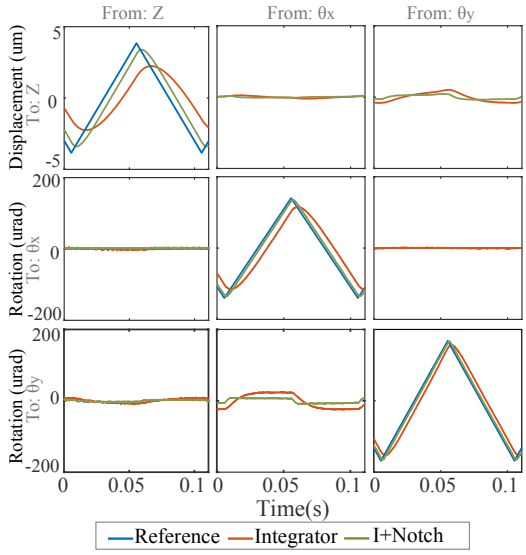

Fig. 8. Closed-loop performances of the decentralized integrator and the combined integrator and notch filter while tracking a 10-Hz triangular reference.

filters are tuned to 1.85 kHz. The tracking performance of a 10-Hz triangular reference in closed-loop is depicted in Fig. 8. The controller with the combined integrator and notch filter provides better tracking than that of the integrator. The results also show a significant reduction in cross-coupling motions. A multivariable control design based on model-less inversion-based techniques is published alongside this paper [26].

VII. Conclusions

This paper proposes a new ultra-thin, five-axis monolithic nanopositioner fabricated from a bimorph sheet of piezoelectric material. The proposed monolithic nanopositioner has a X and Y translational range of 6.2 μm and 5.2 μm respectively, a Z translational range of 26.5 μm, and a rotational range of 600 μrad and 884 μrad about the X- and Y-axis respectively. The Z resonance frequency appears at 845 Hz, and the rotational resonant mode appears at 1850 Hz. A decentralized control strategy with combined integrator and notch filter was implemented to track motions in Z, θ_x and θ_y. The closed-loop system provides good tracking and significantly reduces cross-coupling motions among the three DOFs.

References

[1] Andrew J Fleming and Yuen Kuan Yong. An ultrathin monolithic xy nanopositioning stage constructed from a single sheet of piezoelectric material. *IEEE/ASME Transactions on Mechatronics*, 22(6):2611–2618, 2017.

[2] Y.K. Yong, S.O.R. Moheimani, B.J. Kenton, and K.K. Leang. Invited review article: High-speed flexure-guided nanopositioning: Mechanical design and control issues. *Review of Scientific Instruments*, 83(12), 2012.

[3] Y.K. Yong, S.S. Aphale, and S.O.R. Moheimani. Design, identification, and control of a flexure-based xy stage for fast nanoscale positioning. *IEEE Transactions on Nanotechnology*, 8(1):46–54, 2009.

[4] MS Rana, HR Pota, and IR Petersen. Performance of sinusoidal scanning with mpc in afm imaging. *IEEE/ASME Transactions on Mechatronics*, 20(1):73–83, 2015.

[5] Srinivasa M Salapaka and Murti V Salapaka. Scanning probe microscopy. *IEEE control systems*, 28(2):65–83, 2008.

[6] AJ Fleming, BJ Kenton, and KK Leang. Bridging the gap between conventional and video-speed scanning probe microscopes. *Ultramicroscopy*, 110(9):1205–1214, 2010.

[7] Abu Sebastian, Angeliki Pantazi, Haris Pozidis, and Evangelos Eleftheriou. Nanopositioning for probe-based data storage [applications of control]. *IEEE Control Systems*, 28(4), 2008.

[8] Sandipan Mishra, Joshua Coaplen, and Masavoshi Tomizuka. Precision positioning of wafer scanners segmented iterative learning control for nonrepetitive disturbances [applications of control]. *IEEE control systems*, 27(4):20–25, 2007.

[9] Antoine Ferreira and Constantinos Mavroidis. Virtual reality and haptics for nanorobotics. *IEEE robotics & automation magazine*, 13(3):78–92, 2006.

[10] Zhi-Qiang Fan, Xiu-Wei Li, and Liu. Piezo-assisted in vitro fertilization of mouse oocytes with spermatozoa retrieved from epididymides stored at 4 degree c. *Journal of Reproduction and Development*, pages 0801250035–0801250035, 2007.

[11] Yuen K. Yong, Sachin P. Wadikhaye, and Andrew J. Fleming. High speed single- and dual-stage vertical positioners. *Review of Scientific Instruments*, 87(8):085104, aug 2016.

[12] Gerd Binnig and Douglas PE Smith. Single-tube three-dimensional scanner for scanning tunneling microscopy. *Review of Scientific Instruments*, 57(8):1688–1689, 1986.

[13] Johannes Maess, Andrew J Fleming, and Frank Allgöwer. Simulation of dynamics-coupling in piezoelectric tube scanners by reduced order finite element analysis. *Review of Scientific Instruments*, 79(1):015105, 2008.

[14] Y.K. Yong, B. Ahmed, and S.O.R. Moheimani. A 12-electrode piezoelectric tube scanner for fast atomic force microscopy. *Proceedings of the 2010 American Control Conference, ACC 2010*, pages 4957–4962, 2010.

[15] Y.K. Yong and S.O.R. Moheimani. Collocated z-axis control of a high-speed nanopositioner for video-rate atomic force microscopy. *IEEE Transactions on Nanotechnology*, 14(2):338–345, 2015.

[16] B. J. Kenton and K. K. Leang. Design and control of a three-axis serial-kinematic high-bandwidth nanopositioner. *IEEE/ASME Transactions on Mechatronics*, 17(2):356 – 368, 2012.

[17] S.P. Wadikhaye, Y.K. Yong, B. Bhikkaji, and S.O. Reza Moheimani. Control of a piezoelectrically actuated high-speed serial-kinematic afm nanopositioner. *Smart Materials and Structures*, 23(2), 2014.

[18] Physik Instrumente. *The World of Micro- and NanoPositioning (PI catalog)*. Physik Instrumente, Karlsruhe, Germany, 2016.

[19] S. I. Moore, M. Omidbeike, A. Fleming, and Y. K. Yong. A monolithic serial-kinematic nanopositioner with integrated sensors and actuators. In *2018 IEEE/ASME International Conference on Advanced Intelligent Mechatronics (AIM)*, pages 150–155, July 2018.

[20] Meysam Omidbeike, Yik R Teo, Yuen K Yong, and Andrew J Fleming. Tracking control of a monolithic piezoelectric nanopositioning stage using an integrated sensor. *IFAC-PapersOnLine*, 50(1):10913–10917, 2017.

[21] C. Zhou, Z. Gong, and B. K. Chen. A closed-loop controlled nanomanipulation system for probing nanostructures inside scanning electron microscopes. *IEEE/ASME Transactions on Mechatronics*, 21(3):1233–1241, June 2016.

[22] MJ Brennan. Actuators for active vibration control-tunable resonant devices. *Applied Mechanics and Engineering*, 5(1):63–74, 2000.

[23] Qing-Ming Wang and L. Eric Cross. Constitutive equations of symmetrical triple layer piezoelectric benders. *Ultrasonics, Ferroelectrics, and Frequency Control, IEEE Transactions on*, 46(6):1343–1351, 1999.

[24] Raymond J. Roark, Warren C. Young, and Richard G. Budynas. *Roark's formulas for stress and strain*. McGraw-Hill, New York, 7th ed edition, 2002.

[25] W.T. Thomson. *Theory of Vibration with Applications*. Prentice-Hall, Englewood Cliffs, 3rd edition, 1988.

[26] M. Omidbeike, Arnfinn A Eielsen, Steven I Moore, and Andrew J Fleming. Multivariable model-less feedforward control of a monolithic nanopositioning stage with fir filter inversion. *International Conference on Manipulation, Automation and Robotics at Small Scales (MARSS)*, 2019.